MRI demonstrates glutamine antagonist-mediated reversal of cerebral malaria pathology in mice

Brittany A. Riggle[a,1], Sanhita Sinharay[b,1], William Schreiber-Stainthorp[b], Jeeva P. Munasinghe[c], Dragan Maric[d], Eva Prchalova[e,f], Barbara S. Slusher[e,f], Jonathan D. Powell[g], Louis H. Miller[h,2], Susan K. Pierce[a], and Dima A. Hammoud[b,2]

[a]Laboratory of Immunogenetics, National Institute of Allergy and Infectious Diseases, National Institutes of Health, Rockville, MD 20852; [b]Center for Infectious Disease Imaging, Radiology and Imaging Sciences, Clinical Center, National Institutes of Health, Bethesda, MD 20892; [c]Magnetic Resonance Imaging Research Facility, National Institute of Neurological Disorders and Stroke, National Institutes of Health, Bethesda, MD 20892; [d]Division of Intramural Research, National Institute of Neurological Disorders and Stroke, National Institutes of Health, Bethesda, MD 20892; [e]Johns Hopkins Drug Discovery, Johns Hopkins School of Medicine, Baltimore, MD 21205; [f]Department of Neurology, Johns Hopkins School of Medicine, Baltimore, MD 21205; [g]Department of Oncology, Sidney Kimmel Comprehensive Cancer Research Center, Johns Hopkins University School of Medicine, Baltimore, MD 21287; and [h]Laboratory of Malaria and Vector Research, National Institute of Allergy and Infectious Diseases, National Institutes of Health, Rockville, MD 20852

Contributed by Louis H. Miller, October 23, 2018 (sent for review July 26, 2018; reviewed by Georges Emile Grau and Samuel C. Wassmer)

The deadliest complication of *Plasmodium falciparum* infection is cerebral malaria (CM), with a case fatality rate of 15 to 25% in African children despite effective antimalarial chemotherapy. No adjunctive treatments are yet available for this devastating disease. We previously reported that the glutamine antagonist 6-diazo-5-oxo-L-norleucine (DON) rescued mice from experimental CM (ECM) when administered late in the infection, a time by which mice had already suffered blood–brain barrier (BBB) dysfunction, brain swelling, and hemorrhaging. Herein, we used longitudinal MR imaging to visualize brain pathology in ECM and the impact of a new DON prodrug, JHU-083, on disease progression in mice. We demonstrate in vivo the reversal of disease markers in symptomatic, infected mice following treatment, including the resolution of edema and BBB disruption, findings usually associated with a fatal outcome in children and adults with CM. Our results support the premise that JHU-083 is a potential adjunctive treatment that could rescue children and adults from fatal CM.

cerebral malaria | glutamine antagonist | *Plasmodium falciparum* | MRI | experimental cerebral malaria

Much of Africa is endemically infected with *Plasmodium falciparum* (*Pf*) parasites which give rise to malaria. Malaria presents with periodic fever, chills, and other flu-like symptoms which, after years of repeated exposure, lead to asymptomatic infections (1). For unknown reasons, in a small percentage of patients, many of whom are young children, severe complications can arise, resulting in approximately a half-million deaths each year (2). Cerebral malaria (CM) is the deadliest complication of *Pf* infection (2). The current WHO diagnosis of CM is defined by an unarousable coma in conjunction with a *Pf*-positive peripheral blood smear in the absence of trauma or other coma-causing infections (2–4). Despite treatment with highly effective antimalarial drugs, 15 to 25% of children with CM eventually succumb to the disease (2). Of those who survive, 25% develop long-term neurological sequelae, including epilepsy, blindness, deafness, behavioral disorders, and cognitive impairment (5). Although CM is mostly a disease of young children in areas of intense and stable *Pf* transmission, such as sub-Saharan Africa, in areas of low endemicity, including South and Southeast Asia, CM occurs in both adults and children although the pattern of CM syndromes differs (2, 3). Although CM incidence and subsequent sequelae rates are lower in adults, the case fatality rates are even higher than those reported in children (2, 6). Despite the considerable disease burden, there are no predictive diagnostics or treatments after onset. Furthermore, the molecular mechanisms leading to severe disease remain elusive.

A complete understanding of the pathophysiology of CM has been complicated by a multitude of factors, including the following: the relative rarity of CM (only 2% of *Pf*-infected children develop this complication), the paucity of concentrated "outbreaks," the rapidity of disease progression even with antimalarial treatment (in children, deaths generally occur within 24 to 48 h of admission to regional hospitals), and that infected patient populations live primarily in medical resource-poor countries which lack imaging infrastructure, including MRI scanners. Elucidating disease mechanisms of CM is essential to inform the development of treatments. Thus, the mouse model of CM, experimental CM (ECM), is an essential tool in the search for adjunctive therapies (7). Susceptible mouse strains, including C57BL/6, develop ECM when infected with *Plasmodium berghei* ANKA (*Pb*A) (8) and exhibit pathological changes including cerebral endothelial cell damage with breakdown of the blood–brain barrier (BBB), brain swelling, and hemorrhaging, along with clinical symptoms including paralysis, convulsions, and coma (9–11). The onset of clinical symptoms in our experimental method occurred in the evening of day 5 postinfection (p.i.), but cerebral edema and hemorrhaging were apparent on necropsy as

Significance

Cerebral malaria (CM) is the deadliest complication of *Plasmodium falciparum* infection, resulting in a 15 to 25% mortality rate in African children despite antimalarial chemotherapy. Tragically, nearly a fourth of pediatric CM survivors suffer long-term neurological sequelae. There is an urgent public health and humanitarian need for therapies for CM. In a mouse model of CM, we used magnetic resonance imaging (MRI) to monitor infected mice longitudinally as CM progressed and noninvasively demonstrate that the edema and blood–brain barrier dysfunction, which ultimately result in death, are rapidly reversed by treatment with the glutamine antagonist JHU-083. The similarities between CM MRI shown in mice and those reported in children and adults suggest that glutamine antagonists may be effective CM therapies.

Author contributions: B.A.R., S.S., L.H.M., S.K.P., and D.A.H. designed research; B.A.R., S.S., W.S.-S., J.P.M., and D.M. performed research; E.P., B.S.S., and J.D.P. contributed new reagents/analytic tools; B.A.R., S.S., W.S.-S., L.H.M., and D.A.H. analyzed data; and B.A.R., S.K.P., and D.A.H. wrote the paper.

Reviewers: G.E.G., The University of Sydney; and S.C.W., London School of Hygiene & Tropical Medicine.

Conflict of interest statement: B.S.S. and J.D.P. are founders of Dracen Pharmaceuticals, a company pursuing small molecule glutamine antagonists for clinical oncology applications.

[1]B.A.R. and S.S. contributed equally to this work.

[2]To whom correspondence may be addressed. Email: lmiller@niaid.nih.gov or hammoudd@cc.nih.gov.

This article contains supporting information online at www.pnas.org/lookup/suppl/doi:10.1073/pnas.1812909115/-/DCSupplemental.

Published online December 4, 2018.

early as day 4 p.i. By day 6 p.i., mice began to exhibit seizures, hypothermia, weight loss, severe locomotor deficits, and coma; all infected mice died by the end of day 7 p.i. Although published survival curves indicate that the length of time between infection and death in ECM can be variable and, in some cases, can occur over several days, we and others have reported that death can be relatively synchronous, occurring over a 36-h period, spanning day 6 and 7 p.i. (*SI Appendix*, Fig. S1) (12, 13). MRI provided evidence in vivo that brain edema, both vasogenic and cytotoxic, as well as reduced cerebral blood flow, play dominant roles in death in ECM (14). In general, ECM brain abnormalities described by MRI have been primarily observed in the olfactory bulbs (OBs), but also more posteriorly in the corpus callosum (CC) and subcortical white matter/external capsules in more severe disease (14–18). Subsequent MRI studies provided similar evidence that brain swelling contributed to death in pediatric (19, 20) and adult CM (21). Thus, MRI appears to be a robust tool to investigate the impact of potential CM therapeutics on the pathologies that contribute to death in both ECM and CM.

We recently reported that treatment with the glutamine antagonist 6-diazo-5-oxo-L-norleucine (DON) rescued over 50% of ECM animals, even when administered late in the infection, on day 6 p.i., at a time when the BBB was compromised and brain swelling had occurred (12). This was the only example of a drug that could be given "late" in the disease process, after symptom onset, a common clinical scenario in both pediatric and adult CM. Our findings were consistent with multiple studies demonstrating that glutamine antagonists exhibit promise as neuroprotective agents. Glutamine antagonists have shown potential for treating neuroinflammation in infectious diseases, including HIV-associated neurocognitive disorders, hepatic encephalopathy, neurotropic viral infections, CNS neuroinflammatory diseases, such as multiple sclerosis, and advanced solid brain tumors (22–29). Moreover, increases in the levels of glutamine in the brains of mice infected with *Pb*A have been reported by MR spectroscopy in vivo (17) and by NMR ex vivo (30), suggesting that the modulation of glutamine-dependent events may have therapeutic potential in ECM. Glutamate excitotoxicity modulates BBB integrity (31–33), possibly underlying the pathophysiology of ECM. This, coupled with the fact that glutamine is the major synthetic precursor for glutamate production in the brain, supported our efforts to investigate the potential use of glutamine antagonists as CM therapies.

In this study, we visualized disease progression and drug rescue in *Pb*A-infected mice, in vivo, using high resolution cross-sectional and longitudinal MRI. We compared the structural abnormalities detected in ECM mice to disease manifestations reported in patients, including brain edema and BBB disruption, and correlated those imaging findings with clinical disease progression and histological analysis of brain tissues. For treatment, we used JHU-083 (ethyl 2-(2-amino-4-methylpentanamido)-6-diazo-5-oxohexanoate), an orally available prodrug form of DON developed by Slusher and coworkers (22) to control drug localization and bioavailability based on human metabolism. In an effort to identify effects that can be solely attributed to glutamine antagonists, this study did not employ antimalarial drugs in conjunction with JHU-083.

Results

MRI Comparison of Infected and Uninfected Mice (T_2 Relaxometry and Diffusion-Weighted Imaging). All *Pb*A-infected mice used in these T_2 relaxometry and diffusion-weighted imaging (DWI) scans showed detectable peripheral parasitemia on day 5 p.i. and began exhibiting significant clinical symptomatology on day 6 p.i. All mice succumbed over a 36-h period beginning day 6 p.i. (*SI Appendix*, Fig. S1). In the cross-sectional study, we used T_2 relaxometry and DWI scans from the OBs through the cerebellum (Fig. 1*A*) to assess the accumulation of extracellular fluid in *Pb*A-infected mouse brains compared with healthy, uninfected controls. Typically, T_2 values within a voxel increase when the fluid content in that voxel increases. Qualitatively, T_2-weighted coronal images of infected mice (day 5 and 6 p.i.) showed increased signal in the white matter of the OBs compared with uninfected mice (Fig. 1*B*). In some infected mice, increased T_2 signal was also observed along the posterior white matter tracts, including within and underneath the CC and external capsules. T_2 values obtained from T_2 maps were significantly different between uninfected and infected mice in both the OBs (Kruskal–Wallis test, $P = 0.0068$) and striatum (Kruskal–Wallis test, $P = 0.0022$) (Fig. 2*A*). Post hoc analysis showed that the animals on day 6 p.i. had significantly higher T_2 values in the OBs compared with uninfected animals ($P = 0.025$). In the striatum, day 6 p.i. animals had higher T_2 values than day 5 p.i. animals ($P = 0.012$).

The same group of animals also underwent DWI, from which apparent diffusion coefficient (ADC) maps were derived. On DWI, restricted diffusion in the brain (decreased ADC values) generally reflects cytotoxic edema, such as that seen in ischemia, although other potential causes include increased cellularity or increased fluid viscosity. On the other hand, facilitated diffusion (increased ADC values) is associated with vasogenic edema but

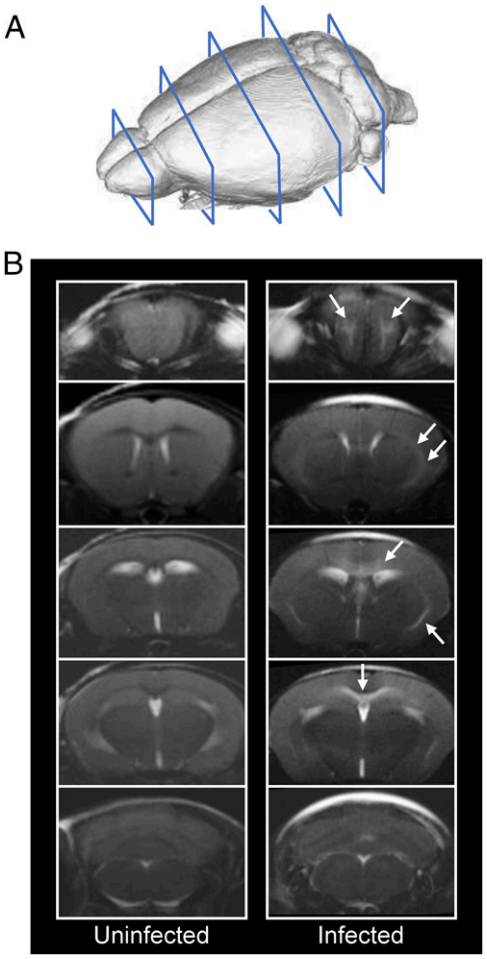

Fig. 1. T_2-weighted coronal images of a mouse brain at multiple planes. (*A*) Diagram showing the planes of imaging in a mouse brain, starting with the olfactory bulbs and continuing through the cerebellum. (*B*) Representative scans of one uninfected mouse and one *Pb*A-infected mouse on day 6 p.i. The infected animal shows high signal intensity in the white matter of the olfactory bulbs, along the corpus callosum (mainly inferior aspect) and the external capsules (white arrows) consistent with edematous changes.

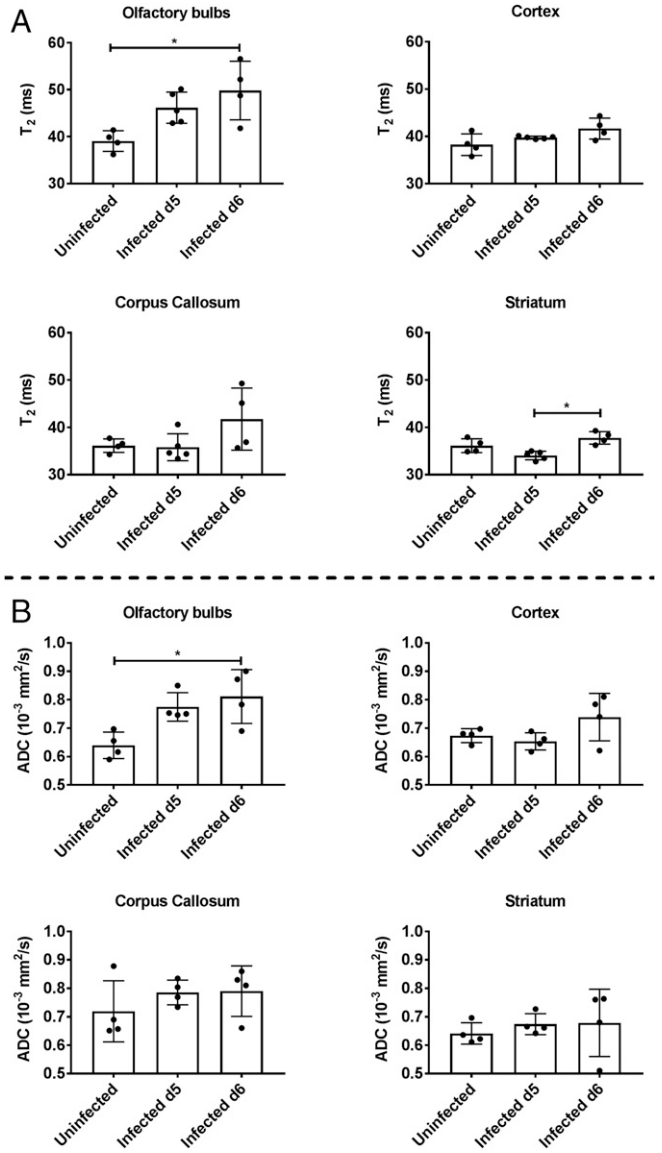

Fig. 2. Quantitative analysis of cross-sectional T_2 relaxometry and ADC values in different regions of the brain. (*A*) Cross-sectional T_2 values for different regions of the brain in uninfected mice ($n = 4$), and mice day 5 p.i. ($n = 5$, average clinical score = 3) and day 6 p.i. ($n = 4$, average clinical score = 4). The olfactory bulbs show a significant increase in T_2 values between uninfected and day 6 p.i. animals (Dunn's post hoc, $P = 0.025$) while the striatum shows a significant increase between day 5 and day 6 p.i. animals (Dunn's post hoc, $P = 0.012$). Kruskal–Wallis analysis: olfactory bulbs, $P = 0.0068$; cortex, $P > 0.1$; corpus callosum, $P > 0.1$; and striatum, $P = 0.0022$. (*B*) Cross-sectional ADC values for different regions of the brain in uninfected mice ($n = 4$) and infected mice day 5 p.i. ($n = 4$, average clinical score = 3) and day 6 p.i. ($n = 4$, average clinical score = 2). The olfactory bulbs show a significant increase in ADC values between uninfected mice and infected mice day 6 p.i. (Dunn's post hoc, $P = 0.043$). Kruskal–Wallis analysis: olfactory bulbs, $P = 0.022$; cortex, $P > 0.1$; corpus callosum, $P > 0.1$; and striatum, $P > 0.1$. Error bars represent mean ± SD. Dunn's post hoc analysis: $^*P < 0.05$.

can also be seen in necrotic or cystic masses and in areas of neuronal loss and gliosis (34). In ECM, the abnormal signal seen on T_2 (Fig. 1*B*) is most suggestive of edema, and, in this context, DWI can help distinguish between vasogenic and cytotoxic edema. ADC values were significantly different between the groups in the OBs (Kruskal–Wallis test, $P = 0.022$). Post hoc analysis showed the main differences to be between uninfected and animals day 6 p.i., with higher ADC values seen in the latter ($P = 0.043$) (Fig. 2*B*). Interestingly, the cerebellum was unique in showing lower ADC values for mice day 5 and 6 p.i. compared with uninfected animals (uninfected, 0.74 ± 0.06; infected day 5 p.i., 0.59 ± 0.03; infected day 6 p.i., 0.68 ± 0.15). This could potentially reflect early ischemic changes related to increased intracranial pressure, mainly in the posterior fossa, with compression of the cerebellar tissues. Although we did not obtain sagittal imaging to show cerebellar compression in our animals, this phenomenon (restricted diffusion) has been described previously with ECM (14).

JHU-083–Treated Mice Show Enhanced Survival. We evaluated the impact of the DON prodrug JHU-083 on ECM. The full pharmacokinetics of JHU-083, including release of the active drug in the mouse brain, have recently been described (35). In our animals, treatment with JHU-083 (*SI Appendix*, Fig. S2) on the morning of day 6 p.i. resulted in ∼60% long-term survival in *Pb*A-infected mice compared with untreated mice (*SI Appendix*, Fig. S1 and Movies S1 and S2). All mice in the untreated group died or reached a clinical score mandating euthanasia by the end of day 6 p.i. through day 7 p.i. (*SI Appendix*, Fig. S1 and Movie S1). Frequently, the JHU-083–treated mice that did not respond to treatment exhibited seizure-like movements and decreased responsiveness to physical stimuli similar to behavior displayed by infected, untreated animals. A group of uninfected animals was also treated with JHU-083 and showed no mortality or other adverse effects. Taken together, these findings indicate that the DON prodrug JHU-083 is as effective in treating CM in this mouse model as we previously demonstrated for DON (12).

MRI Comparison of Uninfected, Untreated, and JHU-083–Treated Mice (T_1-Weighted, with Contrast). Cross-sectional T_1 and postcontrast T_1-weighted images were obtained to assess BBB integrity, with gadolinium (Gd) contrast agent extravasation being indicative of BBB disruption. In infected animals, postcontrast T_1-weighted images showed central abnormal enhancement in the OBs of mice imaged immediately after treatment on day 6 p.i. (white solid arrows, Fig. 3*B*), which was not observed in the uninfected mice (Fig. 3*A*). Abnormal enhancement was also noted more posteriorly involving the CC and external capsules. Interestingly, we saw increased signal within the ventricles after contrast enhancement in both infected and uninfected mice (Fig. 3, white arrowheads). We believe this is due to physiologic leakage of contrast across the blood–cerebrospinal fluid (CSF) barrier due to the long duration of the T_1 acquisition (22 min). A similar process was recently described with leakage of contrast across the blood–CSF barrier in rats starting within 10 min of administration of various contrast agents. Gadopentetate dimeglumine (Magnevist), the contrast agent we used, showed the highest amount of leakage compared with the other contrast materials tested (36). However, the leakage in the infected mice was more prominent, compared with the uninfected mice, although this did not reach significance (Kruskal–Wallis test, $P = 0.051$) (*SI Appendix*, Fig. S4).

The percent signal enhancement was determined in selected regions of the brain of the four animal groups imaged cross-sectionally (Fig. 4). The change in signal intensity after contrast administration was significantly different in the OBs between the groups (Kruskal–Wallis test, $P = 0.0012$). Post hoc analysis showed a significant difference between uninfected and infected, treated animals on day 6 p.i. ($P = 0.0016$) and between animals treated on day 6 p.i. and those receiving two treatments by day 7 p.i. ($P = 0.035$). There were also significant differences between infected and uninfected mice in cortex, CC, and striatum (Fig. 4). In all regions except the CC, the enhancement was significantly lower in treated day 7 p.i. compared with treated day 6 p.i. mice. Taken together, these results demonstrate both accumulation of extracellular fluids and BBB disruption in mice infected with *Pb*A by day 6 p.i., consistent with earlier

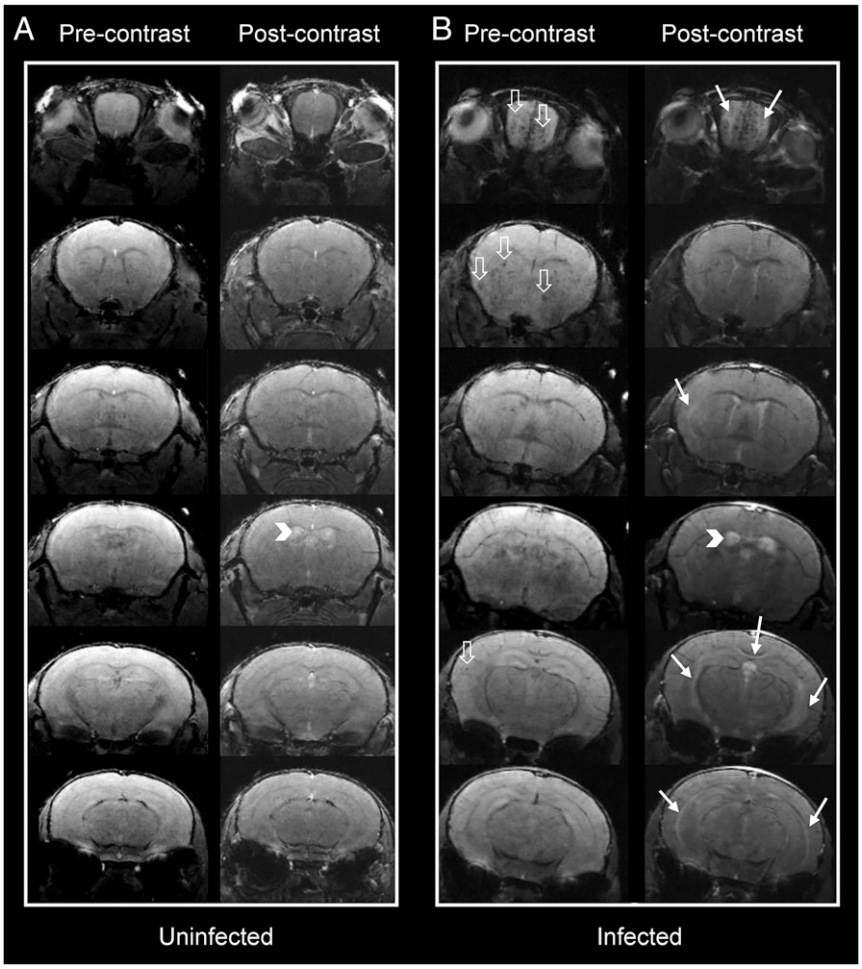

Fig. 3. Pre- and postcontrast coronal T_1 images at different planes in the mouse brain. Representative cross-sectional pre- and postcontrast T_1-weighted images in (*A*) an uninfected and (*B*) an infected mouse. Postcontrast images in the infected animal show increased signal intensity (solid white arrows) in the olfactory bulbs, underneath the corpus callosum, and external capsules. Physiologic contrast leakage into the ventricular system is seen in the uninfected animal due to prolonged imaging time. Ventricular contrast leakage in the infected animal is more marked, suggesting blood–CSF barrier disruption (arrowheads). Multiple microhemorrhagic changes are seen in the infected animal (hollow white arrows).

reports (14, 16). These phenomena are reversed by treatment with JHU-083.

Longitudinal MRI Studies Show JHU-083–Induced Reversal of Brain Pathology. Coronal T_2-weighted images of animals that responded to JHU-083 treatment and survived long-term demonstrated high signal intensity in the OBs and to a lesser extent underneath the CC on day 6 p.i. that resolved by day 8 p.i. T_2-weighted images are shown for a representative mouse (Fig. 5*A*), and T_2 and ADC values for the OBs of six infected animals are plotted graphically (Fig. 5 *B* and *C*). No recurrence of the signal was observed on day 12 p.i. Paired *t* test comparison between mice day 5 and 8 p.i. showed significant decrease of T_2 values in the OBs ($P = 0.043$) but not in the rest of the assessed regions (striatum, cortex, and CC). The changes in ADC values were not significant in any region. This recovery and resolution of abnormal signal corresponded to improvement of clinical symptoms, with the surviving JHU-083–treated animals regaining baseline activity levels and motor skills (Fig. 5*D* and Movies S1 and S2). In some animals, the T_2 values on day 12 p.i. were slightly lower than those seen in uninfected animals. This could be due to minimal, visually unidentifiable microhemorrhagic changes. In contrast, mice that did not respond to treatment did not typically survive past day 6 p.i. and showed more extensive high signal intensity in the OBs, CC, and external capsule compared with treated mice that survived (Fig. 5 *B* and *C*, red circles, *SI Appendix*, Fig. S5). This could reflect advanced pathology indicated by higher T_2 and ADC values that could not be reversed by our drug. However, this will need to be documented in larger samples.

Postcontrast T_1-weighted images demonstrated abnormal enhancement qualitatively in the OBs and multiple other regions of the brain, which decreased on day 8 p.i. and resolved by day 14 p.i. (Fig. 6*A*). This corresponded quantitatively to high percent enhancement in the OBs and to a lesser extent in the cortex, CC, and striatum compared with control values (dotted lines Fig. 6*B*) on day 6 p.i. The abnormal enhancement was significantly reduced by day 8 p.i. in all assessed regions (Fig. 6*B*) (paired *t* test; OBs, $P < 0.0001$; cortex, $P = 0.0038$; CC, $P = 0.0010$; striatum, $P = 0.0017$). Only two animals could be imaged on day 14 p.i. (lack of venous access due to repeated tail vein catheter placements), but, in those animals, the abnormal enhancement did not recur. The resolution of abnormal enhancement corresponded to improved clinical scores (Fig. 6*C*).

Immunohistochemistry Analysis of *Pb*A-Infected Cerebral Tissue from Mice. Brain tissue from uninfected mice, *Pb*A-infected, untreated mice on day 6 p.i., and JHU-083–treated, infected mice on day 8 p.i. were analyzed via immunohistochemistry (IHC) focusing

MICROBIOLOGY

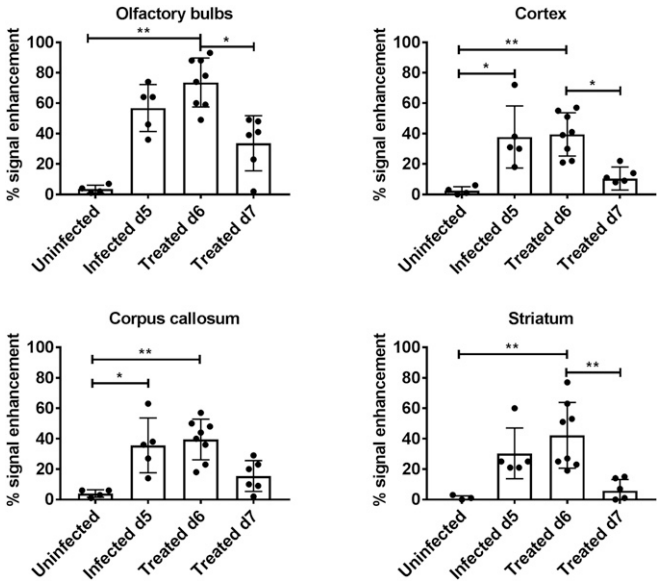

Fig. 4. Quantification of cross-sectional T_1 signal enhancement (between pre- and postcontrast images) in different regions of the brain. Cross-sectional T_1 values shown are for uninfected mice ($n = 4$), day 5 p.i. mice ($n = 5$, average clinical score = 3); post initial treatment, day 6 p.i. mice ($n = 8$, average clinical score = 4); and post second treatment day 7 p.i. mice ($n = 6$, average clinical score = 2). Treated day 6 p.i. animals were scanned immediately following initial treatment on the morning of day 6 p.i., while treated day 7 p.i. animals were imaged 12+ h after receiving second treatment. Kruskal–Wallis analysis: olfactory bulbs, $P = 0.0012$; cortex, $P = 0.0012$; corpus callosum, $P = 0.0031$; and striatum, $P = 0.0008$. Error bars represent mean ± SD. Dunn's post hoc analysis: $*P < 0.05$, $**P < 0.005$.

on a region of interest (ROI) in the OBs (Fig. 7*A*). Mice were infected with a GFP-labeled *Pb*A parasite. Staining for fibrinogen showed multiple patchy areas of positive staining in the infected animals compared with uninfected animals. Those same areas showed an accumulation of red blood cells (RBCs) and positive staining for GFP-labeled parasites within the parenchyma (Fig. 7*B*). There were significant differences in RBC (TER119) staining (Kruskal–Wallis, $P = 0.0036$) and borderline significant differences in fibrinogen staining (Kruskal–Wallis, $P = 0.050$) between the three groups of animals (*SI Appendix*, Fig. S6). Post hoc analysis showed significantly higher TER119 staining on day 6 p.i. compared with uninfected mice ($P = 0.022$). Our findings suggest that, despite reversal of edema and BBB disruption, extravasated RBCs and parasites remain postrecovery in treated animals, although to a lesser extent than in the untreated cohort. This is consistent with our findings of microhemorrhagic changes in the infected animals (open arrows, Fig. 3), despite resolution of abnormal enhancement and abnormal T_2 signal intensity. We did not find any evidence of microglial activation or astrocytosis histologically.

Discussion

Our cross-sectional imaging results of untreated, infected animals are similar to previously reported data: vasogenic cerebral edema, mainly in the OBs but also along white matter tracts, including the CC and external capsule, disruption of BBB with extravasation of contrast material, venous congestion, and microhemorrhagic changes (14–16, 18, 37–39). IHC staining further confirmed our findings, showing protein leakage and extravasation of RBCs, all overlapping with the presence of GFP-labeled parasites in the parenchymally extravasated RBCs. However, we were able to show, in vivo, the reversal of pathological abnormalities under the effect of an experimental CM treatment, a glutamine antagonist, in the brain of ECM mice using longitudinal high-resolution MR imaging. Reversal of brain edema (seen on T_2-weighted images and ADC maps) and BBB disruption (seen on contrast-enhanced T_1-weighted images) in this model was shown qualitatively as well as quantitatively. The resolution of imaging abnormalities corresponded to improvements in the clinical scores of the treated animals.

The pathophysiology of ECM and the drug rescue mechanism of DON/JHU-083 remain unclear. Recent studies of the effect of JHU-083 on the brain in a mouse model of depression-associated behaviors provide some insight into the possible mechanisms by

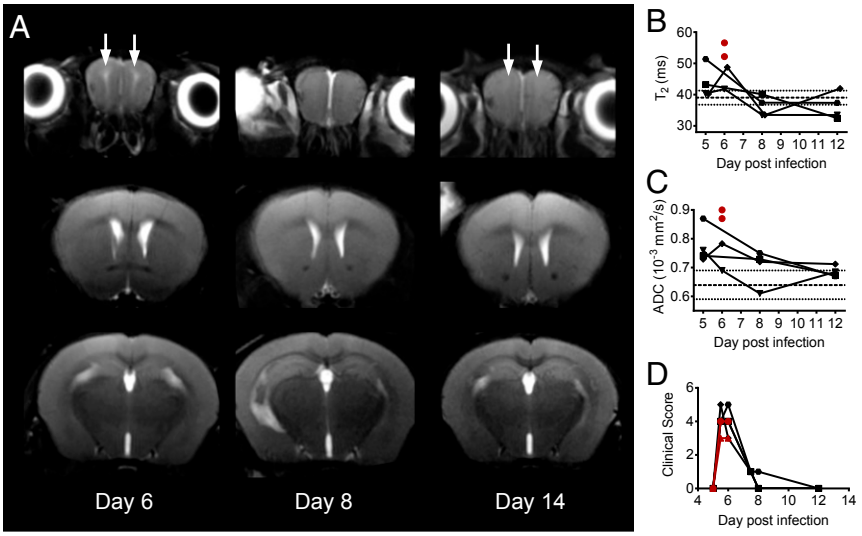

Fig. 5. Longitudinal, coronal, T_2-weighted images of JHU-083–treated animals. (*A*) Coronal T_2-weighted images in a representative animal that survived long-term imaged after treatment at 6:00 AM on day 6 p.i. with JHU-083. Abnormal high signal intensity foci in the OBs appear on day 6 p.i. (solid white arrows) and then resolve by day 12 p.i. (*B*) Quantification of T_2 values and (*C*) ADC values in the OBs of infected animals that responded to treatment ($n = 4$, black symbols) and two that progressed rapidly and did not survive despite treatment ($n = 2$, red circles) are shown. T_2: paired *t* test comparison between day 5 and 8 p.i., $P = 0.043$; and ADC: paired *t* test comparison between day 5 and 8 p.i., $P > 0.05$. Dashed lines denote mean ± SD for T_2 and ADC values in uninfected animals (T_2, 39.1 ± 2.2 and ADC 0.64 ± 0.05). (*D*) Corresponding clinical score data vs. day postinfection for the imaged animals.

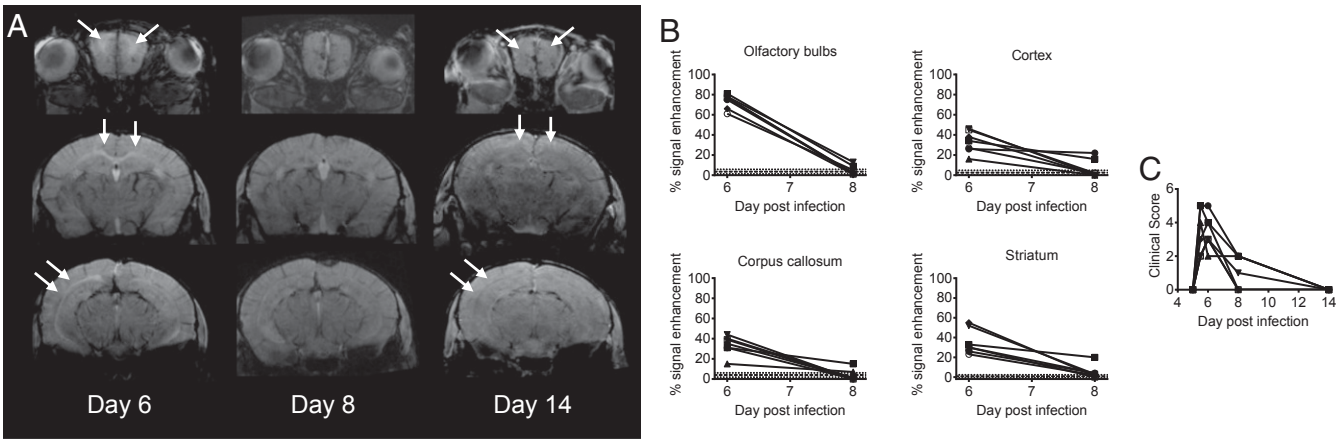

Fig. 6. Longitudinal, coronal postcontrast T_1-weighted images of JHU-083–treated animals. (*A*) Postcontrast T_1-weighted images showing reversal of abnormal enhancement (solid white arrows) in the OBs, CC, and external capsules in a representative treated animal scanned on days 6, 8, and 14 p.i. (*B*) Quantitative decrease in percent signal enhancement for infected animals measured on day 6 and 8 p.i. ($n = 7$). Paired *t* test in the olfactory bulbs, $P < 0.0001$; cortex, $P = 0.0038$; corpus callosum, $P = 0.0010$; and striatum, $P = 0.0017$. Dashed lines denote mean ± SD for uninfected animals in a given region (olfactory bulbs 3.5 ± 2.3; cortex 2.5 ± 2.3; corpus callosum 4.0 ± 2.1; and striatum 0.75 ± 1.5). (*C*) Corresponding clinical scoring vs. day postinfection for the same seven animals. All animals were treated at 6:00 AM on day 6 p.i.

which JHU-083 functions (35). These studies demonstrated that increases in glutaminase activity, specifically in microglia-enriched $CD11b^+$ cells, were normalized by JHU-083. The glutaminase enzyme, which catalyzes the hydrolysis of glutamine to glutamate, is inhibited by JHU-083, resulting in a net decrease of glutamate buildup which has otherwise been associated with neuroinflammation. A previous study also showed that DON blocked glutamate release by activated microglia (40). In ECM, glutamine levels appear to increase (14, 41), suggesting that blocking the function of glutaminase by the glutamine antagonist JHU-083 in ECM could result in a net decrease of glutamate levels in the treated animals. BBB disruption related to glutamate excitotoxicity has been well documented (31–33), and reversal of this mechanism by decreasing glutamate levels in the brains of treated animals probably underlies our observed reversal of BBB disruption and associated improved survival. Another possible contributing factor is related to $CD8^+$ T cell regulation; previous studies in *Pb*A-infected mice have shown that parasite-specific $CD8^+$ T cells interact with the cerebral endothelium, causing inflammation which ultimately results in BBB breakdown, brain swelling, and microhemorrhaging (42). In addition, a multitude of effector function and depletion assays demonstrated the role of $CD8^+$ T cells in ECM pathology (43–47) although the participation of brain-localizing $CD8^+$ T cells in CM remains unresolved.

Although DON and its variants are the first class of therapeutics to show efficacy after symptom onset, we have previously reported a subset of animals that did not improve upon DON treatment (12). Here, we showed that animals which did not respond to treatment had advanced disease with more severe imaging abnormalities, including more extensive posterior edematous changes, compared with animals that responded to treatment. Those changes seem to indicate a certain level of neuropathology beyond which the animal cannot be rescued. Currently, patients generally present to clinic after symptom onset, making therapies that reverse disease manifestations necessary. Our results indicate that such therapies, including JHU-083, need to be administered in a critical window to improve the chances of response in this vulnerable patient population.

The clinical symptoms in the ECM model recapitulate many of those observed in patients with CM, including ataxia, seizure activity, respiratory distress, and coma. Disease progression in mice, as in humans, is rapid, with noticeable deterioration of condition in a single day and death occurring within hours of severe symptom onset. Similarly, the imaging findings in ECM mice are also quite comparable with humans, despite pathoanatomical differences in disease manifestations. In a recent MRI study of pediatric patients with CM, the principal observations included vasogenic cerebral edema and microhemorrhagic changes (48). Vasogenic edema and venous congestion were also shown in a study of both children and adults (21). Seydel et al. (19) reported brain swelling with decreased pre/postpontine CSF levels as the primary finding indicative of poor prognosis in children with CM. Indeed, multiple MRI studies of CM patients have identified specific imaging changes that are predictive of mortality and residual neurological sequelae in survivors (19–21, 49, 50). In one study, increased brain volume was found to be the strongest predictor of fatality, with 84% of children who died presenting with significant cerebral edema on admission (19). These disease manifestations are reminiscent of what we and other groups have observed in the ECM model, including BBB disruption, brain vasogenic edema with increased T_2 and ADC values (as assessed quantitatively in this study), microhemorrhagic changes seen on imaging and confirmed by histopathology, and prominence of deep and superficial venous structures in the infected animals compared with uninfected ones, suggesting venous congestion. Our range of T_2 values in the edematous areas are comparable with those described by Hoffman et al. (16) who also described increased ADC values. Our results were not completely congruent with Penet et al. (14) regarding DWI, however, with their animals mainly showing restricted rather than facilitated diffusion. This could be related to differences in disease progression and/or severity between the two studies.

CM pathophysiology has been investigated extensively, but the exact mechanisms underlying disease progression and molecular pathogenesis remain elusive. Previously, it was widely believed that venous occlusion caused by sequestered infected RBCs (iRBCs) was solely responsible for generating pathology, but mortality remains high even with the implementation of fast-acting antimalarials like artemisinin combination therapies (51–53). There is increasing evidence that both the cerebral vascular sequestration and host immune response contribute to neuropathology (54–56). Ultimately, downward herniation of the brainstem as a result of increased intracranial pressure leads to rapid death in these patients, and the expeditious reversal of this edema may dramatically reduce mortality. Fully understanding disease pathogenesis will inform the development of therapeutics and may also provide clinical indicators for the use of invasive treatments in addition to chemotherapies. Considering the

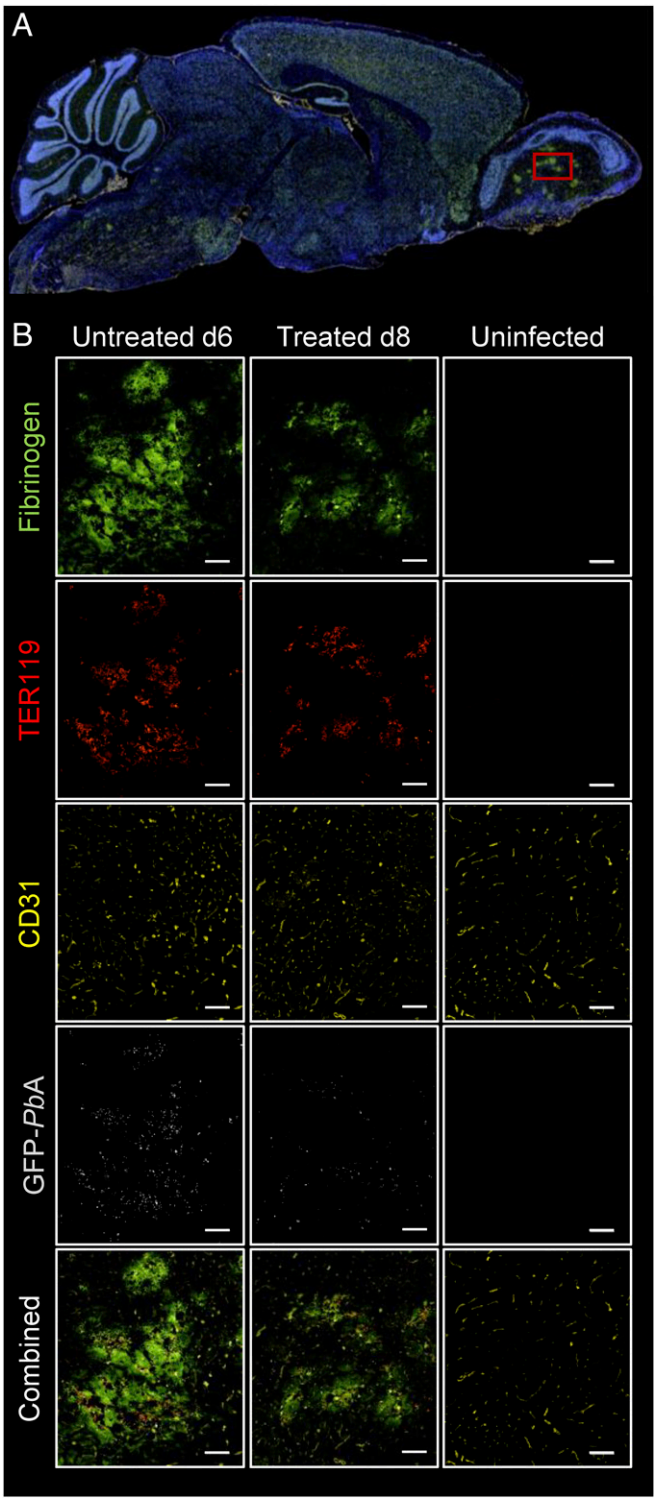

Fig. 7. Immunofluorescent staining of sagittal sections of mice infected with *Pb*A (untreated and treated) and control uninfected mice. (*A*) A representative full sagittal section of the stained mouse brain. (*B*) Magnified images obtained in the olfactory bulbs (red square in *A*) of an infected untreated mouse that was euthanized 6 d p.i. (*Left* column), a treated mouse euthanized 8 day p.i. (*Middle* column), and an uninfected mouse (*Right* column). Positive staining for fibrinogen (bright green), red blood cells (TER119, red), endothelial cells (CD31, yellow), and GFP-labeled parasites (light gray) show evidence of extravascular protein and blood extravasation in both infected mice compared with the control animal. Regions of protein accumulation colocalize with extravasated, parasite-infected RBCs (33.3% magnification). (Scale bar: 100 μm.)

similarities in reported MRI findings between ECM and CM, we believe glutamine antagonists represent a uniquely promising approach for the treatment of a devastating disease course in an especially vulnerable patient population of young children. This work, documenting the in vivo reversal of ECM brain pathology by JHU-083 using high resolution MRI, supports the consideration of this class of therapeutics for clinical trials involving patients with CM.

Methods

Animals. All experiments were performed on 6- to 7-wk-old C57BL/6 female mice from The Jackson Laboratory (JAX 664). This study used 85 animals to initially evaluate drug efficacy. The imaging portion of the study used a total of 45 animals (*SI Appendix*, Table S1). We included day 6 p.i. scans ($n = 4$) from the longitudinal T_2/ADC cohort in the cross-sectional analysis. An additional nine mice were used in the IHC study component.

***PbA* Infection.** A donor animal was infected intraperitoneally (i.p.) with *PbA* from frozen blood stock not more than three passages from mosquito. The parasitemia levels were monitored starting on day 4 p.i. by smear or flow cytometry (described below). When the donor mouse reached a parasitemia of ∼5%, usually by day 5 post infection (p.i.), it was exsanguinated. Blood was diluted in sterile PBS to generate an infection mixture containing 10^6 infected red blood cells per 200 μL. Experimental mice were infected intraperitoneally (i.p.) within 30 min of donor exsanguination. After infection, animals were monitored twice daily on days 1 to 4 p.i., and, beginning on day 5 p.i., animals were scored clinically (1 to 10) to evaluate disease progression according to a standard scoring system, described below. Mice were also evaluated for parasitemia on day 5 p.i. and were excluded from the study if peripheral parasitemia was less than 2%. Our animal protocol mandated an experimental end point for mice with a clinical score greater than six or a parasitemia above 60%. When experimental end points were reached, mice were humanely euthanized (57).

Clinical Score. Infected mice were monitored for the progression of ECM using a 10-point clinical scoring system that rates mice from a score of 0 (no abnormalities) to 10 (moribund) as previously described and adapted from the simple neuroassessment of asymmetric impairment (SNAP) scoring system (58, 59). Briefly, animals were scored by testing five categories: interactions/reflex, cage grasp, visual placing, gait/posture/appearance, and capacity to hold their body weight on a baton. Each category was scored from 0 to 2, where 0 represented normal individuals, 1 intermediate, and 2 no ability to perform described parameter.

Parasitemia. Peripheral parasitemia was determined by flow cytometry using a modification of a previously described method (60). Briefly, 0.6 μL of blood was obtained from mouse tail snip, washed with 2 mL of PBS, resuspended, and stained with the following: Hoechst 33342 (Sigma) DNA dye (8 μM, 1:1,000), dihydroethidium (Sigma) DNA and RNA dye (32 μM, 1:500), and the C57BL/6 lymphocyte marker allophycocyanin (APC)-conjugated Ab specific for CD45 (Biolegend) clone 30-F11 (1:200). Cells were analyzed either on a BD LSRII flow cytometer equipped with UV (325 nm), violet (407 nm), blue (488 nm), and red (633 nm) lasers or on a BD Fortessa ×20 equipped with UV (325 nm), violet (405 nm), blue (488 nm), yellow-green (561 nm), and red (640) lasers. Data were analyzed using FlowJo software (Tree Star Technologies). Infected red blood cells (iRBCs) were CD45-negative, Hoechst-positive, and dihydroethidium-negative. Parasitemia was calculated as the ratio of iRBCs to the total number of RBCs.

Treatment. Mice were treated starting at 6:00 AM on day 6 p.i. with JHU-083, a prodrug version of DON (*SI Appendix*, Fig. S2) (22). Note that JHU-083 is reported as compound **4a** [ethyl 2-(2-amino-4-methylpentanamido)-6-diazo-5-oxohexanoate] in Rais et al. (22). The crystalline JHU-083 was prepared in a 7 mg/mL ethanol stock solution that was then diluted in Hepes buffer to 1.82 mg/kg doses of 200 μL. The stock was prepared fresh at the beginning of each experiment (and stored in solution at −20 °C for no more than 1 wk), and the dose was diluted in 1 M Hepes immediately before treatment. The drug was delivered via oral gavage [per os (PO)]. Animals received a second treatment 12 h later (day 6 p.i., 6:00 PM) and then on days 8 and 10 p.i. at 6:00 AM.

Drug Efficacy. The efficacy of JHU-083 was evaluated before imaging experiments were initiated. Mice were infected as described above and then were separated into two groups: treated with JHU-083 (as described) initiated on day 6 p.i. at 6:00 AM or untreated. The parasitemia was monitored, and

mice were visually evaluated twice daily throughout the course of the experiment. The clinical score was measured on days 5 to 8 p.i. Mice in both groups were euthanized once they reached a clinical score end point of greater than six. Mice in the treated cohort were euthanized if parasitemia reached end point levels of 60% or at study end point of day 22 p.i.

MRI Setup. MRI experiments were carried out on a 30-cm horizontal 9.4 T Bruker-Avance scanner (Bruker Biospin Inc.). Standard MRI protocols were used as in previous ECM studies (14, 16, 17). Animals used for each study type are summarized in *SI Appendix*, Table S1. For the cross-sectional T_2 relaxometry and diffusion-weighted image (DWI) studies, four uninfected mice and nine infected mice were included. Longitudinal T_2 relaxometry and DWI studies were obtained on a subgroup of mice on day 5, 6, 8, and day 12 postinfection ($n = 6$). Quantitative T_2 relaxation maps were derived from the multislice-multiecho (MSME) sequence. Apparent diffusion coefficient (ADC) maps were calculated from DWI scans. While T_2-weighted images show fluid accumulation in the extracellular space as areas of increased signal (and high T_2 values), DWI can discriminate between vasogenic edema (facilitated diffusion, high ADC values) from cytotoxic edema, such as what is seen with ischemic/stroke (restricted diffusion, decreased ADC values). A second group of mice were scanned cross-sectionally using pre- and postcontrast T_1-weighted imaging and included four uninfected; five infected, untreated day 5 p.i.; eight infected, treated day 6 p.i.; and six infected, treated day 7 p.i. mice. Longitudinal T_1 imaging studies were performed on day 5 and day 8 p.i. ($n = 7$). Two of those animals were also imaged at day 14 p.i. but were not included in the quantitative analysis due to the small number of animals. The extravasation of gadolinium-based contrast material through a disrupted BBB usually results in shortening of T_1 values and secondary increased signal intensity on postcontrast compared with precontrast T_1-weighted images. For each imaging session, mice were anesthetized, and the anesthesia plane was maintained using 1.5 to 3.0% isoflurane delivered in 1 L/min oxygen gas ventilation (61). Animals were secured in a custom-built, MRI-compatible, stereotaxic holder and were placed on a water circulating heating block connected to a water bath. To maintain core body temperature at 37.0 ± 0.2 °C, a circulating water heater (SA instruments, Inc.) and rectal probe were used. A pressure transducer (SA Instruments, Inc.) was used to monitor respiration rate. Isoflurane levels were modulated as necessary to maintain the respiratory rate at 40 ± 10 breaths per minute similar to what has been previously described (62), to prevent motion artifacts. The stereotaxic holder/heating block was fitted into a custom-built cradle, and an 86-mm volume (transmit) per 4 mouse head array (receive) radio frequency coil ensemble was centered over the animal's skull. The entire cradle was then centered in the scanner. For enhanced T_1 imaging, gadopentetate dimeglumine (Magnevist) (0.2 mmol/kg) was diluted 1:5 in 0.9% sodium chloride and was injected 5 min before the scan via tail vein catheter (63). The volume of delivered prepared contrast solution was ∼0.2 mL After scanning, mice were given an s.c. saline injection and placed on a heating pad to recover. Infected mice underwent clinical scoring and parasitemia measurements on day 5 p.i. before imaging and were included in the scan group if parasitemia levels had reached at least 2%. All treated animals received initial treatment at 6:00 AM on day 6 p.i. To minimize total time under anesthesia and in the scanner, separate groups were used for T_1 studies and T_2 relaxometry/ADC studies.

MRI Sequences. MRI sequences were as follows. For T_2, axial T_2 relaxometry MR images were acquired with varying echo times using a multislice-multiecho (MSME) sequence with the following imaging parameters: repetition time (TR)/echo time (TE) = 3,700 ms/15 ms, number of echoes = 16, field of view (FOV) = 1.92 cm × 1.92 cm, matrix size = 128 × 128, slice thickness = 1 mm, number of averages = 2, number of slices = 13 to 14, and total in-plane resolution 150 μm. The total scan time was 16 min. For DWI, multislice diffusion weighted spin-echo echoplanar imaging was used with TR/TE = 2,000 ms/24.5 ms, number of slices = 13 to 14, slice thickness = 1 mm, FOV = 1.92 cm × 1.92 cm, matrix size = 128 × 128, and two averages for each direction (x, y, and z) with total in-plane resolution of 150 μm and total scan duration of 42 min. For T_1, pre- and postcontrast Magnevist injection, 3D T_1-weighted images were acquired using a fast recovery sequence, driven equilibrium Fourier transform (DEFT) with the following MR parameters: TR/TE = 2,348 ms/5 ms, inversion time (TI) = 2,150 ms, number of slices = 34 to 36, slice thickness = 0.4 mm, FOV = 1.92 cm × 1.92 cm, matrix size = 256 × 256, flip angle = 30°, number of averages = 2, total in-plane resolution of 75 μm, and total scan duration of 22 min. Post gadolinium (Gd) T_1-weighted MR images were acquired 5 min after injection of the contrast.

MRI Data Analysis. MRI data were processed and quantitatively analyzed using Matlab (R2016b) (Mathworks Inc.) and ParaVision 5.1. T_2 values were calculated from quantitative maps generated from fitting the T_2 image to an exponential decay using the equation $S_i = M_0 \exp(-TE/T_2) + C$, where S_i = signal intensity, M_0 = net magnetization at equilibrium, and C = offset constant (64, 65). Regions of interest (ROIs) were drawn manually on fitted T_2 maps, in selected regions of the brain including the following: olfactory bulbs (OBs), cortex, corpus callosum (CC), and striatum *SI Appendix*, Fig. S3. Finally, all ROI values corresponding to a given region were averaged to generate the average T_2 value for that region. ADC values for the same regions in the brain were obtained from the average of the DWI acquired along three orthogonal directions (ADCx, ADCy, and ADCz). For each direction, ADC values were generated in a pixel-wise manner from manually drawn pixels of the same area, using the equation $\ln[S_i(b)/S_i(b=0)] = -b \times ADCi$, where S is the signal intensity, i = x, y, z directions, and $b = \gamma^2 G^2 \delta^2 (\Delta - \delta/3)$ where G and δ are the magnitude and duration of the gradient pulses, respectively, and Δ is the time interval between them (66). Pre- and post-Gd T_1-weighted signal intensities were calculated using ParaVision 5.1. ROIs were drawn on the slices corresponding to OBs, cortex, CC, and striatum for the pre-Gd image. The ROIs were selected to include commonly involved regions based on ECM literature (OBs and CC), as well as other areas (cortex and striatum) with potential quantitative, even if not qualitative, changes. Additional ROIs were selected in the ventricles to assess for contrast leakage across the blood–CSF barrier and in the cerebellum to assess for possible early brain herniation and compression of the posterior fossa structures. The ROIs were then cloned on the postcontrast images for the same animal, and mean signal intensity values were generated for both scans. Since the pre- and postcontrast images are coregistered and the sequence parameters are identical, the change in signal intensity within the same ROIs can be used as a surrogate for contrast leakage, which would result in increased signal (67, 68). The changes in signal intensity before and after Gd infusion were then calculated as follows: [(Post-Gd intensity − Pre-Gd intensity)/Pre-Gd intensity] × 100.

Immunohistochemistry Tissue Preparation. Multiplex fluorescence immunohistochemistry was performed on 10-μm-thick frozen sections sourced from uninfected and *PbA*-GFP–infected mice, perfused with 4% paraformaldehyde in PBS and cryoprotected with sucrose. Tissue was embedded in optimal cutting temperature (OCT) compound, sagittally sliced, and mounted by HistoServ, Inc. Antigen unmasking was performed using standard heat-mediated antigen retrieval in 10 mM citrate buffer, pH 6.0. The sections were incubated with F_c receptor blocking solution (Innovex Biosciences) to saturate endogenous F_c receptors and then in Background Buster solution (Innovex Biosciences) to minimize nonspecific antibody binding, per the manufacturer's instructions. The sections were then immunoreacted for 1 h at room temperature using 1 μg/mL cocktail mixture of the following immunocompatible primary antibodies: chicken IgY anti-green fluorescent protein (GFP) to amplify detection of *PbA*-GFP parasites (parasites were kindly provided by W. Heath, University of Melbourne, Victoria, Australia), rabbit IgG anti-fibrinogen to detect leaky blood vessels in the brain parenchyma, and a mixture of directly conjugated anti-mouse CD31-Alexa Fluor 647 and anti-mouse TER-119-PerCP, to label endothelial cells and extravasated RBCs, respectively (69). Next, excess primary antibodies were removed with PBS supplemented with 1 mg/mL BSA. The sections were stained using a 1 μg/mL cocktail mixture of the following highly cross-adsorbed secondary antibodies (Thermo Fisher, Jackson ImmunoResearch, or Li-Cor Biosciences): goat anti-chicken IgY-Alexa Fluor 488 and goat anti-rabbit IgG-Alexa Fluor 430. After washing off excess secondary antibodies, sections were counterstained using 100 ng/mL DAPI (Thermo Fisher Scientific) for visualization of cell nuclei. Slides were then coverslipped using Immu-Mount medium (Thermo Fisher Scientific) and imaged using a multichannel wide field epifluorescence microscope (see below).

Image Acquisition. Images were acquired from whole specimen sections using the Axio Imager.Z2 slide scanning fluorescence microscope (Zeiss) equipped with a 20×/0.8 Plan-Apochromat (Phase-2) nonimmersion objective (Zeiss), a high resolution ORCA-Flash4.0 sCMOS digital camera (Hamamatsu), a 200W X-Cite 200DC broad band lamp source (Excelitas Technologies), and five customized filter sets (Semrock) optimized to detect the following fluorophores: DAPI, Alexa Fluor 430, Alexa Fluor 488, Alexa Fluor 546, and PerCP. Image tiles (600 × 600-mm viewing area) were individually captured at 0.325 μm per pixel spatial resolution, and the tiles were seamlessly stitched into whole specimen images using the ZEN 2 image acquisition and analysis software program (Zeiss), with an appropriate color table having been applied to each image channel to either match its emission spectrum or to

set a distinguishing color balance. Pseudocolored stitched images were then exported to Adobe Photoshop and overlaid as individual layers to create multicolored merged composites. After staining was performed on sagittal sections, analysis was completed using ImageJ. Regions of interest were drawn to encompass the entirety of the OBs. The percentage of the ROI that was positive for the marker of interest (TER119 or fibrinogen) was calculated. The percent area covered was compared across groups.

Statistics. Statistical analysis of the imaging results was done using GraphPad Prism 7. Even though our data were parametric, we used the more conservative Kruskal–Wallis nonparametric method to analyze differences in ADC values, T_2 values, and changes in T_1 signal intensities between the animal groups. For the longitudinal analysis, we used a paired *t* test.

Study Approval. Animals were housed and maintained according to standards of the Association for Assessment and Accreditation of Laboratory Animal Care. All studies were approved by the Animal Care and Use Committee of the National Institutes of Health.

ACKNOWLEDGMENTS. We thank the Mouse Imaging Facility at the National Institutes of Health. This research was supported by the Intramural Research Program of the NIH National Institute of Allergy and Infectious Diseases, Laboratory of Immunogenetics and by the Center for Infectious Diseases, Clinical Center, NIH. Funding support for JHU-083 development was from the Bloomberg Kimmel Institute for Cancer Immunotherapy (E.P., B.S.S., and J.D.P.). The content of this publication does not necessarily reflect the views or policies of the Department of Health and Human Services or does the mention of trade names, commercial products, or organizations imply endorsement by the US Government.

1. World Health Organization (2015) *World Malaria Report* (WHO, Geneva).
2. WHO (2014) Severe malaria. *Trop Med Int Health* 19:7–131.
3. Wassmer SC, et al. (2015) Investigating the pathogenesis of severe malaria: A multidisciplinary and cross-geographical approach. *Am J Trop Med Hyg* 93(Suppl):42–56.
4. Taylor TE (2009) Caring for children with cerebral malaria: Insights gleaned from 20 years on a research ward in Malawi. *Trans R Soc Trop Med Hyg* 103:S6–S10.
5. Mishra SK, Newton CRJC (2009) Diagnosis and management of the neurological complications of falciparum malaria. *Nat Rev Neurol* 5:189–198.
6. Hawkes M, Elphinstone RE, Conroy AL, Kain KC (2013) Contrasting pediatric and adult cerebral malaria: The role of the endothelial barrier. *Virulence* 4:543–555.
7. Craig AG, et al.; participants of the Hinxton Retreat meeting on Animal Models for Research on Severe Malaria (2012) The role of animal models for research on severe malaria. *PLoS Pathog* 8:e1002401.
8. Randall LM, et al. (2008) Common strategies to prevent and modulate experimental cerebral malaria in mouse strains with different susceptibilities. *Infect Immun* 76: 3312–3320.
9. Thumwood CM, Hunt NH, Clark IA, Cowden WB (1988) Breakdown of the blood-brain barrier in murine cerebral malaria. *Parasitology* 96:579–589.
10. Miu J, et al. (2008) Chemokine gene expression during fatal murine cerebral malaria and protection due to CXCR3 deficiency. *J Immunol* 180:1217–1230.
11. Potter S, et al. (2006) Perforin mediated apoptosis of cerebral microvascular endothelial cells during experimental cerebral malaria. *Int J Parasitol* 36:485–496.
12. Gordon EB, et al. (2015) Targeting glutamine metabolism rescues mice from late-stage cerebral malaria. *Proc Natl Acad Sci USA* 112:13075–13080.
13. Strangward P, et al. (2017) A quantitative brain map of experimental cerebral malaria pathology. *PLoS Pathog* 13:e1006267.
14. Penet MF, et al. (2005) Imaging experimental cerebral malaria in vivo: Significant role of ischemic brain edema. *J Neurosci* 25:7352–7358.
15. Saggu R, Faille D, Grau GE, Cozzone PJ, Viola A (2011) In the eye of experimental cerebral malaria. *Am J Pathol* 179:1104–1109.
16. Hoffmann A, et al. (2016) Experimental cerebral malaria spreads along the rostral migratory stream. *PLoS Pathog* 12:e1005470.
17. Penet MF, et al. (2007) Magnetic resonance spectroscopy reveals an impaired brain metabolic profile in mice resistant to cerebral malaria infected with Plasmodium berghei ANKA. *J Biol Chem* 282:14505–14514.
18. Zhao H, et al. (2014) Olfactory plays a key role in spatiotemporal pathogenesis of cerebral malaria. *Cell Host Microbe* 15:551–563.
19. Seydel KB, et al. (2015) Brain swelling and death in children with cerebral malaria. *N Engl J Med* 372:1126–1137.
20. Potchen MJ, et al. (2012) Acute brain MRI findings in 120 Malawian children with cerebral malaria: New insights into an ancient disease. *AJNR Am J Neuroradiol* 33: 1740–1746.
21. Mohanty S, et al. (2017) Magnetic resonance imaging of cerebral malaria patients reveals distinct pathogenetic processes in different parts of the brain. *MSphere* 2: e00193-17.
22. Rais R, et al. (2016) Discovery of 6-diazo-5-oxo-L-norleucine (DON) prodrugs with enhanced CSF delivery in monkeys: A potential treatment for glioblastoma. *J Med Chem* 59:8621–8633.
23. Lee CF, et al. (2015) Preventing allograft rejection by targeting immune metabolism. *Cell Rep* 13:760–770.
24. Nedelcovych MT, et al. (2017) N-(pivaloyloxy)alkoxy-carbonyl prodrugs of the glutamine antagonist 6-diazo-5-oxo-L-norleucine (DON) as a potential treatment for HIV associated neurocognitive disorders. *J Med Chem* 60:7186–7198.
25. Rama Rao KV, Norenberg MD (2014) Glutamine in the pathogenesis of hepatic encephalopathy: The trojan horse hypothesis revisited. *Neurochem Res* 39:593–598.
26. Unger C, et al. (2011) A phase I schedule optimization study of pegylated glutaminase (PEG-PGA) plus 6-diazo-5-oxo-l-norleucine (DON) in patients (pts) with advanced solid tumors. *J Clin Oncol* 29(15_Suppl):3049.
27. Manivannan S, Baxter VK, Schultz KLW, Slusher BS, Griffin DE (2016) Protective effects of glutamine antagonist 6-diazo-5-oxo-L-norleucine in mice with alphavirus encephalomyelitis. *J Virol* 90:9251–9262.
28. Potter MC, Figuera-Losada M, Rojas C, Slusher BS (2013) Targeting the glutamatergic system for the treatment of HIV-associated neurocognitive disorders. *J Neuroimmune Pharmacol* 8:594–607.
29. Potter MC, et al. (2015) Neurological sequelae induced by alphavirus infection of the CNS are attenuated by treatment with the glutamine antagonist 6-diazo-5-oxo-l-norleucine. *J Neurovirol* 21:159–173.
30. Le Moyec L, et al. (1997) Brain metabolites in mice coinfected with Plasmodium berghei ANKA and LP-BM5 virus: Assessment by proton magnetic resonance spectroscopy. *Exp Parasitol* 85:296–298.
31. Janigro D, West GA, Nguyen TS, Winn HR (1994) Regulation of blood-brain barrier endothelial cells by nitric oxide. *Circ Res* 75:528–538.
32. Sharp CD, et al. (2003) Human neuroepithelial cells express NMDA receptors. *BMC Neurosci* 4:28.
33. Lee KE, Kang YS (2018) l-Citrulline restores nitric oxide level and cellular uptake at the brain capillary endothelial cell line (TR-BBB cells) with glutamate cytotoxicity. *Microvasc Res* 120:29–35.
34. Padhani A (2009) Unresectable hepatocellular carcinoma: Serial early vascular and cellular changes after transarterial chemoembolization. *Radiology* 250:324–326.
35. Zhu X, et al. (August 13, 2018) JHU-083 selectively blocks glutaminase activity in brain CD11b+ cells and prevents depression-associated behaviors induced by chronic social defeat stress. *Neuropsychopharmacology*, 10.1038/s41386-018-0177-7.
36. Jost G, et al. (2017) Penetration and distribution of gadolinium-based contrast agents into the cerebrospinal fluid in healthy rats: A potential pathway of entry into the brain tissue. *Eur Radiol* 27:2877–2885.
37. Kennan RP, et al. (2005) Reduced cerebral blood flow and N-acetyl aspartate in a murine model of cerebral malaria. *Parasitol Res* 96:302–307.
38. Fauconnier M, et al. (2011) Protein kinase C-theta is required for development of experimental cerebral malaria. *Am J Pathol* 178:212–221.
39. von Zur Muhlen C, et al. (2008) A contrast agent recognizing activated platelets reveals murine cerebral malaria pathology undetectable by conventional MRI. *J Clin Invest* 118:1198–1207.
40. Thomas AG, et al. (2014) Small molecule glutaminase inhibitors block glutamate release from stimulated microglia. *Biochem Biophys Res Commun* 443:32–36.
41. Miranda AS, et al. (2010) Increased levels of glutamate in the central nervous system are associated with behavioral symptoms in experimental malaria. *Braz J Med Biol Res* 43:1173–1177.
42. Swanson PA, 2nd, et al. (2016) CD8(+) T cells induce fatal brainstem pathology during cerebral malaria via luminal antigen-specific engagement of brain vasculature. *PLoS Pathog* 12:e1006022.
43. Nitcheu J, et al. (2003) Perforin-dependent brain-infiltrating cytotoxic CD8+ T lymphocytes mediate experimental cerebral malaria pathogenesis. *J Immunol* 170: 2221–2228.
44. Hermsen C, van de Wiel T, Mommers E, Sauerwein R, Eling W (1997) Depletion of CD4+ or CD8+ T-cells prevents Plasmodium berghei induced cerebral malaria in end-stage disease. *Parasitology* 114:7–12.
45. Claser C, et al. (2011) CD8+ T cells and IFN-γ mediate the time-dependent accumulation of infected red blood cells in deep organs during experimental cerebral malaria. *PLoS One* 6:e18720.
46. Belnoue E, et al. (2002) On the pathogenic role of brain-sequestered alphabeta CD8+ T cells in experimental cerebral malaria. *J Immunol* 169:6369–6375.
47. Yañez DM, Manning DD, Cooley AJ, Weidanz WP, van der Heyde HC (1996) Participation of lymphocyte subpopulations in the pathogenesis of experimental murine cerebral malaria. *J Immunol* 157:1620–1624.
48. Potchen MJ, et al. (2018) 1.5 Tesla magnetic resonance imaging to investigate potential etiologies of brain swelling in pediatric cerebral malaria. *Am J Trop Med Hyg* 98:497–504.
49. Kampondeni SD, et al. (2013) MRI findings in a cohort of brain injured survivors of pediatric cerebral malaria. *Am J Trop Med Hyg* 88:542–546.
50. Postels DG, et al. (2014) Brain MRI of children with retinopathy-negative cerebral malaria. *Am J Trop Med Hyg* 91:943–949.
51. Haldar K, Murphy SC, Milner DA, Taylor TE (2007) Malaria: Mechanisms of erythrocytic infection and pathological correlates of severe disease. *Annu Rev Pathol* 2:217–249.
52. de Souza JB, Hafalla JCR, Riley EM, Couper KN (2010) Cerebral malaria: Why experimental murine models are required to understand the pathogenesis of disease. *Parasitology* 137:755–772.
53. Taylor TE, et al. (2004) Differentiating the pathologies of cerebral malaria by postmortem parasite counts. *Nat Med* 10:143–145, and erratum (2004) 10:435.
54. Small DS, et al. (2017) Evidence from a natural experiment that malaria parasitemia is pathogenic in retinopathy-negative cerebral malaria. *eLife* 6:e23699.
55. van der Heyde HC, Nolan J, Combes V, Gramaglia I, Grau GE (2006) A unified hypothesis for the genesis of cerebral malaria: Sequestration, inflammation and hemostasis leading to microcirculatory dysfunction. *Trends Parasitol* 22:503–508.

56. Villaverde C, Namazzi R, Shabani E, Opoka RO, John CC (2017) Clinical comparison of retinopathy-positive and retinopathy-negative cerebral malaria. *Am J Trop Med Hyg* 96:1176–1184.
57. National Research Council (2011) Guide for the Care and Use of Laboratory Animals (National Academies Press, Washington, DC), 8th Ed.
58. Waisberg M, Vickers BK, Yager SB, Lin CK, Pierce SK (2012) Testing in mice the hypothesis that melanin is protective in malaria infections. *PLoS One* 7:e29493.
59. Shelton SB, et al. (2008) A simple, efficient tool for assessment of mice after unilateral cortex injury. *J Neurosci Methods* 168:431–442.
60. Malleret B, et al. (2011) A rapid and robust tri-color flow cytometry assay for monitoring malaria parasite development. *Sci Rep* 1:118.
61. Hildebrandt IJ, Su H, Weber WA (2008) Anesthesia and other considerations for in vivo imaging of small animals. *ILAR J* 49:17–26.
62. Guo J, et al. (2018) In vivo detection and automatic analysis of GABA in the mouse brain with MEGA-PRESS at 9.4 T. *NMR Biomed* 31:e3837.
63. Lohöfer F, et al. (2018) Molecular imaging of myocardial infarction with Gadofluorine P–A combined magnetic resonance and mass spectrometry imaging approach. *Heliyon* 4:e00606.
64. Zheng S, Xia Y (2010) On the measurement of multi-component T2 relaxation in cartilage by MR spectroscopy and imaging. *Magn Reson Imaging* 28:537–545.
65. Milford D, Rosbach N, Bendszus M, Heiland S (2015) Mono-exponential fitting in T2-relaxometry: Relevance of offset and first echo. *PLoS One* 10:e0145255.
66. van Gelderen P, et al. (1994) Water diffusion and acute stroke. *Magn Reson Med* 31: 154–163.
67. Piazza M, et al. (2017) Simulating vasogenic brain edema using chronic VEGF infusion. *J Neurosurg* 127:905–916.
68. Navarathna DHMLP, et al. (2013) MRI confirms loss of blood-brain barrier integrity in a mouse model of disseminated candidiasis. *NMR Biomed* 26:1125–1134.
69. Lundie RJ, et al. (2008) Blood-stage Plasmodium infection induces CD8+ T lymphocytes to parasite-expressed antigens, largely regulated by CD8alpha+ dendritic cells. *Proc Natl Acad Sci USA* 105:14509–14514.